

A strategy of using temporary space-holders to increase the capacity for Li-S batteries

Zhu Mingyang^{a, †}, Nannan Wang^{a, †}, Jun Wang^{a, *}, Jiang Zinan^a, Jiarui Huang^{a, *},
Terence Xiaoteng Liu^{b, *}

^a Key Laboratory of Functional Molecular Solids, Ministry of Education, Anhui Provincial Engineering Laboratory for New-Energy Vehicle Battery Energy-Storage Materials, College of Chemistry and Materials Science, Anhui Normal University, Wuhu 241002, P.R. China

^b Department of Mechanical & Construction Engineering, Faculty of Engineering and Environment, Northumbria University, Newcastle upon Tyne NE1 8ST, U.K.

Corresponding authors: jrhuang@mail.ahnu.edu.cn (J.R. Huang), junjun81@mail.ahnu.edu.cn (J. Wang) and terence.liu@northumbria.ac.uk (X.T. Liu).

† Equal contribution as the first author.

Abstract: The porous structure within the cathode material influences the capacity and operating performance of Li-S batteries. Here, we prepared special carbon material using sodium chloride as template/temporary space-holders to design mixture of micro-/meso-/macroporous structure with large surface area through a facile water bath and freeze-drying process. Such modification led to a high sulfur content of 73.2 % with remarkable initial capacity of 1378 mAh g⁻¹ at 0.1 A g⁻¹, and maintains 48.6% after 100 cycles. Moreover, the Li-S battery displayed superior rate capability of 807 mAh g⁻¹ at 1.0 A g⁻¹. This abundant micro-/meso-/macropores can improve the content of sulfur, relieve the loss of sulfur and exhibit superior cycling performance and rate capability.

Keywords: Micro-/meso-/macroporous; Carbon; rGO; Lithium-sulfur battery

1. Introduction

As energy-storage devices, Li-S batteries drawn more and more attention because of their high capacity, nature abundance and low cost [1-3]. However, some issues should to be solved to improve its applications, such as poor conductivity, shuttle effect and the slow redox reactions [4-6]. Furthermore, the severe volume change in the cycle process damage the structural integrity and limit cyclic stability [7,8].

To overcome these limitations, many carbonaceous materials can induce a better uniform distributed sulfur particle, such as meso/microporous carbon [9], reduced graphene oxide (rGO) [10], carbon nanotubes (CNTs) [11] have used as sulfur carrier. Especially, their superior specific surface area and tunable pore size [12], the micropores of porous carbon can accommodate volumetric change during the discharge process and inhibit the polysulfides dissolving in organic electrolytes [13]. For instance, Liang et al. prepared porous carbon nanotubes, which exhibited 511 mAh g⁻¹ at 1.675 A g⁻¹ over 500 cycles [14]. Wang et al. designed porous carbon using a hydrothermal method, it presented 908 mA h g⁻¹ at 0.167 A g⁻¹ over 100 cycles [15]. However, traditional carbonaceous materials usually prepared by hydrothermal method, have an open porous structure with a pore size of up to micrometers [16], which will lead to unsuccessful blocking of the porous surface and dissolution of the cathode as well as the shuttle effect of polysulfides.

Template method is generally quite simple method to synthesize porous carbon. Many templates such as carbonate [17], silica [18] and molecular sieves [19] have been acted in the preparation of the nanostructured porous carbon. Gao et al. reported a

porous hollow carbon aerogel by using nano-CaCO₃ as template. The composite cathode exhibits 252.5 mA h g⁻¹ at 1.675 A g⁻¹ over 500 cycles [20]. Gu and his co-workers synthesized a porous carbon bulk network by using SiO₂ nanospheres as templates, the composite as a sulfur host exhibits 760 mA h g⁻¹ over 150 cycles at 0.167 A g⁻¹ [21]. However, most introduced porous carbon hosts suffered from low content of sulfur due to their unsatisfactory surface structure such as low specific surface area.

Based on the above considerations, graphene/sulfur composite comes into sight for cathode materials. The rGO with a mass of functional groups, such as hydroxyl groups, carbonyl groups, and carboxyl groups [22-24], generate strong chemical interaction with sulfur, rGO/S cathode can effectively fix the sulfur particles and polysulfide intermediates, limit the dissolution of polysulfides [25]. For instance, Zhou and co-workers designed a porous graphene framework via a vacuum filtration method, which employed for Li-S batteries delivered 728 mA h g⁻¹ over 200 cycles at 0.335 A g⁻¹ [26]. Yang et al. synthesized graphene@sulfur composites by a microwave method, which delivered a capacity of 751 mAh g⁻¹ at 0.335 A g⁻¹ over 80 cycles [27]. Nevertheless, a serious problem is the oxygen containing functional coatings is up to the micrometer scale in thickness [28], it still remains a challenge to improving the conductivity of the graphene.

Starch is a high molecular carbohydrate, which is polymerized by glucose molecules. The starch is an abundant biopolymer in nature, which can be obtained from various plants, such as potato, corn, rice, and wheat. As a biomass carbon source, the starch is low-cost and friendly to the environment. The carbonization of starch releases water vapor, carbon dioxide and carbon monoxide, forming porous carbon with high

purity. Furthermore, sodium chloride (NaCl) nanoparticles can be used as temporary space holders and produce a large number of special macropores in the porous carbon material. In addition to the low price of NaCl, it is also easy to remove with water.

Herein, a facile and scalable strategy was designed to prepare a porous carbon-rGO with abundant micro-/meso- and macropores. The micro-/meso- and macroporous carbon-rGO (MMMPC-rGO) was obtained using starch as carbon source, using NaCl as the temporary space holders, via a facile water bath heating, freeze-drying process and a subsequent heat treatment. When applied in sulfur host, the MMMPC-rGO/S composite demonstrates a high reversible capacity and a superior rate performance. The outstanding electrochemical performance is mainly benefit from the effects of nano-size, conductive carbon networks and porosities.

2. Experimental

2.1 Preparation of MMMPC-rGO and MPC-rGO composites

Graphite oxide was obtained using the Hummers' method described supplementary information [29]. Then the graphite oxide (80 mg) was added into distilled water followed by sonicate for 2 h. Secondly, sodium chloride (NaCl, 0.6 g) and the starch (3.0 g) were sequentially added to the as-prepared rGO solution followed by sonicate for ten minutes. Then, the above solution was put into a water bath, maintained at 80 °C for 60 min. A gelatinous mixture was obtained and it was freeze-dried at -55 °C for 72 h. The mixture was heated at 750 °C for 120 min in N₂ atmosphere. Then, NaCl was leached using distilled water and dried at 110 °C for 120 min. Finally, the micro-/meso- and macropores carbon-rGO (MMMPC-rGO) sample was obtained. For comparison, microporous carbon doped with rGO (MPC-rGO) was synthesized through similar process without NaCl.

2.2 Preparation of cathode materials

Briefly, the as-prepared products and sulfur powder (1:3) were mixed by manual mixing. The mixtures were heated at 165 °C for 30 h in Ar-filled atmosphere. Therefore, the MMMPC-rGO/S and MPC-rGO/S composites were obtained.

2.3 Li-S batteries assembly and material characterization (see SI).

3 Results and discussion

3.1 Characterization

The preparation process of MMMPC-rGO composite is presented in Fig. 1. First, the rGO solution was obtained via ultrasonic dispersion of the graphite oxide solution. Subsequently, sodium chloride and starch were put into the above rGO solution followed by ultrasonic mixing, water bath heating and freeze-drying, forming a gelatinous precursor with NaCl as the pore-forming agent. Second, the gelatinous precursor was carbonized at a high temperature of 750 °C for 2 h in N₂ atmosphere. Finally, the NaCl was leached via washing the sample with distilled water, resulting in porous carbon-rGO with abundant micropores, mesopores and macropores.

Scanning electron microscopy (SEM) images of the samples are shown in Fig. 2 and Fig. S1. Observing from Fig. S1, we can find that the products consist of some microplates with rough surface. Figs. 2a,b show the SEM images of MMMPC-rGO/NaCl sample, some of which look like cubic NaCl particles embedded in the composite. Energy dispersive X-ray spectroscopy (EDS) results shown in Fig. S2a confirms the existences of Na and Cl elements in the composite. The MMMPC-rGO with numerous macropores and the homogeneous pore sizes distribution with average size of 500 nm can be observed (Figs. 2c,d), indicating that cubic NaCl particles were successfully leached out after washing with distilled water, resulting in the porous

structure. It is well consistent with the EDS result of the MMMPC-rGO after washing with distilled water (Fig. S2b). Moreover, EDS was also performed to investigate the elements in the MMMPC-rGO/S composite shown in Fig. S2c, indicating the co-existence of carbon and sulfur elements. High-resolution transmission electron microscopy (HRTEM) images (Figs. 2e,f) also demonstrates the micro-/meso-/macroporous structure of the sample. The inset image presents the selected area electron diffraction (SAED) pattern of MMMPC-rGO, two rings presents (104) and (116) of the hexagonal structure [30].

As shown in Figs. 3a and b, MPC-rGO displayed a wrinkled laminar structure with stacks of some massive blocks. No macropores can be observed because no sodium chloride was added in the preparation process. TEM and HRTEM images (Figs. 3c and d) confirm the microporous structure and amorphous phase of the product.

Fig. 4a presents Brunner–Emmet–Teller (BET) results for MMMPC-rGO composite. The isotherm curves of MMMPC-rGO are a combination of Type I and Type IV isotherms [31]. Observing from the inset of Fig. 4a, MMMPC-rGO contains pores sizes ranging sizes from 0.308 to 28.4 nm, verifying the existence of micropores, mesopores and macropores. The specific surface area and total pore volume of MMMPC-rGO are ca. $438.6 \text{ m}^2 \text{ g}^{-1}$ and $0.269 \text{ cm}^3 \text{ g}^{-1}$, respectively. As for MPC-rGO, they are ca. $352.4 \text{ m}^2 \text{ g}^{-1}$ and $0.193 \text{ cm}^3 \text{ g}^{-1}$, respectively (Fig. S3). Therefore, large surface area and porous structure of the MMMPC-rGO could hold large sulfur loading and capture polysulfides, and the mesopores and macropores can facilitate charge transfer [32].

Fig. 4b shows the X-ray diffraction (XRD) patterns of samples. The diffraction peaks of the MMMPC-rGO/NaCl at 27.3°, 45.4°, 56.4°, and 75.2° are perfectly indexed to the (111), (220), (222) and (420) planes and can be assigned to NaCl (JCPDS no. 75-0306), indicating the presence of cubic phase NaCl [33]. However, after washing with distilled water, these peaks completely disappeared, suggesting complete removal of NaCl from the MMMPC-rGO. As for the XRD pattern of the MMMPC-rGO shown in Fig. 3b, a broad peak at ca. 26° can be observed, which attributes to the (002) plane of amorphous carbon [34]. As for the XRD pattern of the MMMPC-rGO/S composite, the characteristic peaks are similar with the peaks of sulfur powder, and the intensities of diffraction peaks are weaker than those of the pure sulfur powder, indicating the MMMPC-rGO material has been combined with sulfur powder. The peaks of sulfur powder are consistent with the characteristic peaks of orthorhombic sulfur (JCPDS no. 08-0247) [35]. Meanwhile, the broad peak of carbon at ca. 26° disappeared also suggests the MMMPC-rGO and sulfur have been combined successfully [36].

To investigate the chemical states of the elements in the MMMPC-rGO/S, X-ray photoelectron spectroscopy (XPS) measurement was performed. Fig. 5a shows the survey spectrum of MMMPC-rGO/S composites, demonstrating the existence of C, O and S elements. C1s spectrum (Fig. 5b) exhibits three peaks located at 284.7, 286.3 and 289.6 eV, assigning to C-C, C-O and O-C=O bonds, respectively [37]. Part of GO was reduced during the calcination process, resulting a lower peak of oxygen-containing functional groups [17,38]. O 1s spectrum (Fig. 5c) is fitted into two bonds including S-O (532.5 eV) and C-O-C (533.8 eV), respectively [39]. As shown in Fig. 5d, S 2p_{3/2}

(164.2 eV) and S $2p_{1/2}$ (164.9 eV) peaks can be obtained [40]. These chemical bonds within the MMMPC-rGO/S composite can effectively trap the sulfur particles and relieve the diffusion of polysulfide in the redox process [38,41].

Raman spectrum was generally performed to describe the structural characteristic of the carbonaceous materials. As shown in Fig. 6a, the three small peaks below 510 cm^{-1} are corresponding to the peak of sulfur [42], indicating the sulfur was combined to MMMPC-rGO. In addition, two peaks at 1337 and 1594 cm^{-1} come from the D and G bands of carbon [43,44]. D band presents the defect of the carbon, while G band is assigned to graphitic carbon atoms. The value of I_D/I_G for MMMPC-rGO is 0.90, indicating its graphite structure, facilitating the charge transfer in the redox process [45,46]. The defects can enhance the sulfur loading in MMMPC-rGO [39,42,47]. Moreover, the I_D/I_G value of MMMPC-rGO is lower than that of MMMPC-rGO/S (0.91), confirming that the MMMPC-rGO/S composite possesses more lattice defects. Observing from the Raman spectra of MPC-rGO/S, MPC-rGO (Fig. S4), similar results can be obtained. To further investigate the content of sulfur in the MMMPC-rGO/S composite, thermogravimetric analysis (TGA) was conducted at a heating rate of $10\text{ }^\circ\text{C min}^{-1}$ from room temperature to $800\text{ }^\circ\text{C}$ in the air. Fig. 6b shown the sulfur load among the MMMPC-rGO/S is approximately 73.2%. While the sulfur load among the MPC-rGO/S is ca. 69.7%. Furthermore, sulfur loss at $200\text{--}400\text{ }^\circ\text{C}$, and the additional loss from $400\text{ }^\circ\text{C}$ can be ascribed to the oxidation of the MMMPC-rGO and MPC-rGO in air [48].

3.2 Electrochemical properties

Fig. 7a exhibited the cyclic voltammetry (CV) curves of MMMPC-rGO/S composite at 0.1 mV s^{-1} . For the 1st cycle, one peak at ca. 2.42 V corresponds to the transforms of S_8 to Li_2S_n . Another peak at ca. 1.98 V is ascribed to the reduction of Li_2S_n to $\text{Li}_2\text{S}_2/\text{Li}_2\text{S}$. In addition, one peak (2.24 V) is attributed to the oxidation of Li_2S to polysulfides. From the second cycle, the peak shifts to 2.41 V, which is due to the anode reaction [49]. Two peaks presented at approximately 2.24 and 2.01 V are corresponding to the reduction of S_8 to Li_2S_n and $\text{Li}_2\text{S}/\text{Li}_2\text{S}_2$, respectively [50-52]. Compared with the first reduction reaction process at approximately 2.24 V, the second reaction process at approximately 2.01 V involves more lithium ions. Therefore, the area of the reduction peak at 2.01 V is larger than that of the reduction peak at 2.24 V. For the comparison, Fig. S5 exhibited the CV curves of the MPC-rGO/S composite. Similar reduction and oxidation peaks can be observed from Fig. S5.

Fig. 7b illustrated the discharge/charge profiles of the MMMPC-rGO/S. The capacities are 1378, 1331, 1303, 822 and 668 mAh g^{-1} for the 1st, 2nd, 3rd, 50th and 100th cycles. The discharge platforms and charge platform are approximately consistent with the CV peaks. Moreover, the MPC-rGO/S cathode also delivered good rate capacities as shown in Fig. S6. Fig. 7c shows the rate capabilities of MMMPC-rGO/S and MPC-rGO/S. The initial capacities of MMMPC-rGO/S cathode are 1367 mAh g^{-1} at 0.1 A g^{-1} , 1078 mAh g^{-1} at 0.2 A g^{-1} , 920 mAh g^{-1} at 0.5 A g^{-1} and 807 mAh g^{-1} at 1.0 A g^{-1} , and backing to 1054 mAh g^{-1} at 0.1 A g^{-1} . For comparison, the MPC-rGO/S cathode delivered capacities of 792, 513, 433 and 339 mAh g^{-1} from 0.1 to 1.0 A g^{-1} .

Fig. 7d exhibits the performances of the MMMPC-rGO/S and MPC-rGO/S

electrodes at 0.1 A g^{-1} . The MMMPC-rGO/S delivers an initial capacity of 1378 mAh g^{-1} . In contrast, MPC-rGO/S composite exhibits only 837 mAh g^{-1} . Fig. 7e shows the cycling performances of the MMMPC-rGO/S and MPC-rGO/S electrodes at 0.5 A g^{-1} . The first discharge capacity of the MMMPC-rGO/S is 1043 mAh g^{-1} , and the MPC-rGO/S composite exhibits only 640 mAh g^{-1} . The capacity of MMMPC-rGO/S composite maintains 673 mAh g^{-1} over 200 cycles. Moreover, the discharge/charge profiles of the MMMPC-rGO/S composite at 0.5 A g^{-1} are shown in Fig. S7a. As shown in Fig. 7f, MMMPC-rGO/S composite possessed an initial capacity of 852 mAh g^{-1} and retained 597 mAh g^{-1} after 500 cycles. The discharge/charge profiles of the MMMPC-rGO/S composite at 1.0 A g^{-1} are shown in Fig. S7b. The capacity of MMMPC-rGO/S cathode is high, indicating that the sodium chloride as temporary space-holders can anchor polysulfides [53]. Furthermore, the cyclic performance of MMMPC-rGO/S is compared with PC aerogel/GO [54], N-doped GO/PC [55] N-doped GO/metal oxide [56], and other materials etc. [57-60], the comparison of the cycling performance of just mentioned carbonaceous materials served as sulfur carriers are listed in Table S1. Although significant progress has been reported in the corresponding literature, the excellent electrochemical capabilities of MMMPC-rGO/S electrode mainly due to the following aspects. First, the large surface area of MMMPC-rGO may enhance sulfur load and capture polysulfides during charge/discharge process. Second, the micropores can provide containers for immobilizing sulfur and polysulfides. Finally, the coexistences of micro-/meso-/macroporous structure can relieve the shuttle effect via effectively capture polysulfides.

Fig. 8a exhibits the CV curves of the MMMPC-rGO/S cathode at serials scanning rates. The relationship of several mechanisms can be analyzed according to:

$$i = aV^b \quad (1)$$

$$\log i = b \log v + \log a \quad (2)$$

where i is the current, and v represent scan rate, a and b are constant. The process of charge-storage controlled by the diffusion when $b=0.5$, and if $b=1.0$ presents the capacitive-controlled behavior [61-63]. Fig. 8b shows the anodic and cathodic peaks, the values of the slopes are 0.609 and 0.863, respectively, indicating the MMMPC-rGO electrode process is capacitive-controlled behavior. The contribution ratio at each scan rate is demonstrated in Fig. 8c. Moreover, when scan rate at 1 mV s^{-1} , capacitive contribution ratio reaches up to 82.8%, demonstrating micro-/meso-/microporous structure can facilitate the transfer of Li^+ and increase the discharge capacity. The Li^+ diffusion coefficient (D_{Li^+}) was calculated from the CV curves using the Randles-Sevcik equation (3). As shown in Fig. 8d, the peak currents (I_p) of the anodic peak (peak1) and cathodic peak (peak 2) change linearly with the square root of scanning rate ($v^{1/2}$):

$$I_p = 2.69 \times 10^5 n^{3/2} A D^{1/2} C v^{1/2} \quad (3)$$

here n represents number of electrons in per reaction ($n=2$), A represents contact area ($A=1.13 \text{ cm}^2$), and C_{Li^+} is the Li^+ concentration in the electrode ($C_{\text{Li}^+} = 1.0 \times 10 \text{ mol cm}^{-3}$) [64,65]. The MMMPC-rGO cathode exhibits the D_{Li^+} values of peak 1 and peak 2 were 2.24×10^{-10} and $1.98 \times 10^{-12} \text{ cm}^2 \text{ s}^{-1}$, respectively [25,66].

The impedance measurements were carried out by applying an AC amplitude of 5 mVrms on an equilibrium potential of 2.3 V (vs. Li/Li⁺) over the frequency range of 10 mHz to 100 kHz. Electrochemical impedance spectroscopy (EIS) curves before and after 500 cycles are shown in Fig. 9, the insets correspond to the equivalent circuit models for MMMPC-rGO/S and MPC-rGO/S electrodes. The Nyquist plots (Fig. 9a) are consisted of a semicircle and a slanted line. The semicircle is attributed to the charge-transfer resistance (R_{ct}) between cathode materials and electrolyte, and the slanted line is corresponded to Li⁺ diffusion [67]. The MMMPC-rGO/S and MPC-rGO/S electrodes exhibit two semicircles (Fig. 9b) after cycling test. The new semicircle corresponds to SEI film resistance (R_2) [68,69]. Table S2 exhibited the fitting results of MMMPC-rGO/S and MPC-rGO/S electrodes. The value of R_{ct} for the MMMPC-rGO/S cathode is 67.16 Ω before cycling test. After cycles, the R_{ct} values are 1.42 Ω and 14.96 Ω for MMMPC-rGO/S, MPC-rGO/S electrodes, respectively. After 500 cycles, the R_{ct} value is smaller than that of fresh electrode which means that the micro-/meso-/microporous structure with high specific surface area resulting in a promoted transmission of Li ion [70]. For the MMMPC-rGO cathode, the micropores can enhance content sulfur, capture the polysulfides. Moreover, meso-macropores can charge transfer and facilitate electrolyte infiltration [4,38,71]. Therefore, the MMMPC-rGO with micro-/meso-/macropores exhibit superior electrochemical performances.

4. Conclusions

Herein, an MMMPC-rGO composite consisting of the micro-/meso-/macroporous carbon doped with reduced graphene oxide is synthesized via a simple water bath,

freeze-drying and heat treatment. With using sodium chloride as the pore-forming agents, the electrochemical performance has been greatly improved. The MMMPC-rGO/S composite with 73.2 wt% sulfur delivers an initial capacity of 1043 mAh g⁻¹ at 0.2 A g⁻¹, and it retains 750 mAh g⁻¹ over 100 cycles. The outstanding performances are ascribed to the micro-/meso-/macroporous structure in the internal of MMMPC-rGO. Porous carbon exhibits an excellent mechanical flexibility. Moreover, the porous structure can increase S load and relieve the shuttle effect. The introduced graphene-based material can form conductive networks and improve rate performance.

Acknowledgements

Natural Science Research Project for Universities in Anhui Province (KJ2018B14), Science and Technology Major Project of Anhui Province (18030901093), Key Research and Development Program of Wuhu (2019YF07).

Appendix A Supplementary data

Supplementary data to this article can be found online at

References

- [1] G. Tarquini, A. Dell'Era, P.P. Prosini, F.A. Scaramuzzo, F.A. Scaramuzzo, C. Lupi, M. Pasquali, Polysulfide solution effects on LiS batteries performances, *J. Electroanal. Chem.* 870 (2020) 114239.
- [2] L.L. Gao, J. Yang, X.J. Lu, H.B. Ren, E.H. Sheng, J.R. Huang, Hierarchical porous carbon doped with high content of nitrogen as sulfur host for high performance lithium–sulfur batteries, *J. Electroanal. Chem.* 878 (2020) 114593.
- [3] N.N. Wang, J. Wang, J.J. Zhao, J.H. Wang, J.Q. Pan, J.R. Huang, Synthesis of

porous-carbon@reduced graphene oxide with superior electrochemical behaviors for lithium-sulfur batteries, *J. Alloys Compd.* 851 (2020) 156832.

[4] Z.W. Wang, S.P. Wang, Synergistic suppression of the shuttle effect and absorption of electrolytes using a functional rich amine porous organic polymer/acetylene black-polypropylene separator in Li-S batteries, *Electrochim. Acta* 306 (2019) 229–237.

[5] Z.H. Luo, G.B. Zhu, L.K. Yin, F.J. Li, B.B. Xu, L. Dala, X.T. Liu, K. Luo, A facile surface preservation strategy for the lithium anode for high-performance Li-O₂ batteries, *ACS Appl. Mater. Inter.* 12 (2020) 27316–27326.

[6] N.N. Wang, Y. Hong, X.T. Liu, Q. Wang, J.R. Huang, Sucrose derived microporous-mesoporous carbon for advanced lithium-sulfur batteries, *Ceram. Int.* 47 (2021) 899-906.

[7] W.J. Lin, G.Q. He, Y.H. Huang, X.Y. Chen, 3D hybrid of Co₉S₈ and N-doped carbon hollow spheres as effective hosts for Li-S batteries, *Nanotechnology* 31 (2020) 035404.

[8] K.P. Yang, J.J. Yan, R.Y. He, D. Li, Y. Li, T. Li, B.Z. Ren, Nitrogen-doped porous carbon was prepared from peony shell for the cathode material of lithium-sulfur battery, *J. Electroanal. Chem.* 861 (2020) 113922.

[9] Q. Tang, H.Q. Li, M. Zuo, J. Zhang, Y.Q. Huang, P.W. Bai, J.Q. Xu, Optimized assembly of micro-/meso-/macroporous carbon for Li-S batteries, *Nano* 12 (2017) 1750021.

[10] Z.H. Yin, S.Y. Pan, Q. Cheng, G.Z. Zhang, X.Y. Yu, Z.X. Pan, H.S. Rao, X.H. Zhong, Mild-method synthesised rGO-TiO₂ as an effective polysulphide-barrier for lithium-sulphur batteries, *J. Alloys Compd.* 836 (2020) 155341.

- [11] J.Y. Wang, W.J. Wang, Y.G. Zhang, Y. Wang, Y. Zhao, Synthesis of CoO nanocrystals decorated porous carbon nanotube microspheres as sulfur host for high performance Li/S batteries, *Nanotechnology* 31 (2020) 025403.
- [12] S.Y. Yuan, J.L. Bao, L. Wang, Y.Y. Xia, D.G. Truhlar, Y.G. Wang, Graphene-supported nitrogen and boron rich carbon layer for improved performance of lithium-sulfur batteries due to enhanced chemisorption of lithium polysulfides, *Adv. Energy Mater.* 6 (2016) 1501733.
- [13] G.J. Hu, C. Xu, Z.H. Sun, S.G. Wang, H.M. Cheng, F. Li, W.C. Ren, 3D graphene-foam-reduced-graphene-oxide hybrid nested hierarchical networks for high-performance Li-S batteries, *Adv. Mater.* 28 (2016) 1603–1609.
- [14] W.H. Liang, Y.K. Tang, L. Liu, C.X. Zhu, R. Sheng, Effective trapping of polysulfides using functionalized thin-walled porous carbon nanotubes as sulfur hosts for lithium-sulfur batteries, *Inorg. Chem.* 59 (2020) 8481-8486.
- [15] Z.F. Wang, X.M. Zhang, X.L. Liu, Y.G. Zhang, W.M. Zhao, Y.Y. Li, C.L. Qin, Z. Bakenov, High specific surface area bimodal porous carbon derived from biomass reed flowers for high performance lithium-sulfur batteries, *J. Colloid Interf. Sci.* 569 (2020) 22–33.
- [16] H.L. Gao, Y.B. Zhu, L.B. Mao, F. C. Wang, X.S. Luo, Y.Y. Liu, Y. Lu, Z. Pan, J. Ge, W. Shen, Y.R. Zheng, L. Xu, L.J. Wang, W.H. Xu, H.A. Wu, S.H. Yu, Super-elastic and fatigue resistant carbon material with lamellar multi-arch microstructure, *Nat. Commun.* 7 (2016) 12920.

- [17] Y.B. Dong, T. Lan, X. Wang, Y. Zhang, L.Z. Jiang, X.N. Sui, Preparation and characterization of soy protein microspheres using amorphous calcium carbonate cores, *Food Hydrocolloid* 107 (2020) 105953.
- [18] M. Prokopowicz, A. Szewczyk, A. Skwira, R. Sądej, G. Walker, Biphasic composite of calcium phosphate-based mesoporous silica as a novel bone drug delivery system, *Drug Deliv. Transl. Re.* 10 (2020) 455–470.
- [19] M.C. Duke, J.C. Diniz, G.Q. Lu, M. Petch, P. Gray, Carbonised template molecular sieve silica membranes in fuel processing systems: permeation, hydrostability and regeneration, *J. Membrane Sci.* 241 (2004) 325–333.
- [20] X.G. Gao, Y. Huang, H. Gao, S. Batool, M.W. Lu, X. Li, Y.Q. Zhang, Sulfur double encapsulated in a porous hollow carbon aerogel with interconnected micropores for advanced lithium-sulfur batteries, *J. Alloys Compd.* 834 (2020) 155190.
- [21] H.Y. Gu, R. Zhang, P. Wang, S.M. Xie, C.M. Niu, H.K. Wang, Construction of three-dimensional ordered porous carbon bulk networks for high performance lithium-sulfur batteries, *J. Colloid Interf. Sci.* 533 (2019) 445–451.
- [22] C. Vallés-García, E. Montero-Lanzuela, S. Navalona, M. Álvaro, A. Dhakshinamoorthy, H. Garcia, Tuning the active sites in reduced graphene oxide by hydroquinone functionalization for the aerobic oxidations of thiophenol and indane, *Mol. Catal.* 493 (2020) 111093.
- [23] L. Zhou, X.J. Lin, T. Huang, A.S. Yu, Binder-free phenyl sulfonated graphene/sulfur electrodes with excellent cyclability for lithium sulfur batteries, *J. Mater. Chem. A* 2 (2014) 5117.

- [24] J.P. Rong, M.Y. Ge, X. Fang, C.W. Zhou, Solution ionic strength engineering as a generic strategy to coat graphene oxide (GO) on various functional particles and its application in high-performance lithium–sulfur (Li–S) batteries, *Nano Lett.* 14 (2014) 473–479.
- [25] L.L. Gao, Y.X. Cao, J. Wang, H.B. Ren, J.H. Wang, J.R. Huang, Construction of polypyrrole coated hollow cobalt manganate nanocages as an effective sulfur host for lithium-sulfur batteries, *Ceram. Int.* 46 (2020) 18224–18233.
- [26] Z. Zhou, Z.X. Wang, J.W. Ji, K. Fu, C.C. Cao, J.W. Yang, Y.M. Xue, C.C. Tang, Uniform embedding of ultrafine sulfur into well-honeycombed porous graphene frameworks for highly stable Li–S batteries, *Mater. Lett.* 276 (2020) 128243.
- [27] W. Yang, W. Yang, S.L. Di, G. Sun, X.J. Qin, Exploring effective approach to synthesize graphene@sulfur composites for high performance lithium-sulfur batteries, *Curr. Nanosci.* 14 (2018) 335-342.
- [28] S.Y. Bai, X.Z. Liu, K. Zhu, S.C. Wu, H.S. Zhou, Metal–organic framework-based separator for lithium–sulfur batteries, *Nat. Energy* 1 (2016) 16094.
- [29] X.J. Lu, D.X. Liu, T.L. Han, M.Y. Zhu, S.O. Ryu, J.R. Huang, A facile synthesis of sandwich-structured SnS₂@reduced graphene oxide with high performance for lithium-ion battery anode, *J. Alloys Compd.* 765 (2018) 1061-1071.
- [30] S.G. Shinde, M.P. Patil, G.–D. Kim, V.S. Shrivastava, Ni, C, N, S multi–doped ZrO₂ decorated on multi–walled carbon nanotubes for effective solar induced degradation of anionic dye, *J. Environ. Chem. Eng.* 8 (2020) 103769.
- [31] D.P. Li, X.H. Ren, Q. Ai, Q. Sun, L. Zhu, Y. Liu, Z. Liang, R.Q. Peng, P.C. Si, J.

- Lou, J.K. Feng, L.J. Ci, Facile fabrication of nitrogen-doped porous carbon as superior anode material for potassium-ion batteries, *Adv. Energy Mater.* 8 (2018) 1802386.
- [32] Z.R. Tao, J.R. Xiao, H. Wang, F.W. Zhang, Novel cathode structure based on spiral carbon nanotubes for lithium-sulfur batteries, *J. Electroanal. Chem.* 851 (2019) 113477.
- [33] A.M. Abraham, S.V. Kumar, S.M. Alhassan, Porous sulphur copolymer for gas-phase mercury removal and thermal insulation, *Chem. Eng. J.* 332 (2018) 1-7.
- [34] W.H. Liang, Y.K. Tang, L. Liu, C.X. Zhu, R. Sheng, Effective trapping of polysulfides using functionalized thin-walled porous carbon nanotubes as sulfur hosts for lithium-sulfur batteries, *Inorg. Chem.* 59 (2020) 8481-8486.
- [35] G.F. Chen, J.H. Li, N. Liu, Y. Zhao, J.G. Tao, G. Kalimuldina, Z. Bakenov, Y.G. Zhang, Synthesis of nitrogen-doped oxygen-deficient TiO_{2-x} /reduced graphene oxide/sulfur microspheres via spray drying process for lithium-sulfur batteries, *Electrochim. Acta* 326 (2019) 134968.
- [36] G. Radhika, P. Rajkumar, R. Subadevi, M. Sivakumar, Manganese and graphene oxide composite as highly effective sulfur host for enlightening electrochemical kinetics of lithium-sulfur batteries, *Int. J. Energy Res.* (2020) 1-10. DOI:10.1002/er.6136.
- [37] X.M. Li, Q.L. Zhu, W.M. Guo, Q.H. Lu, The catalytic activity of manganese dioxide supported on graphene promoting the electrochemical performance of lithium-sulfur batteries, *J. Electroanal. Chem.* 840 (2019) 144-152.
- [38] X.B. Chen, Y. Wang, Y.C. Wang, J.Y. Huang, Z.Z. Ye, A hierarchical high-porosity graphene oxide porous carbon/sulfur composite with sodium chloride as temporary

space-holders for high performance lithium-sulfur batteries, *Chemelectrochem* 6 (2019) 2667–2674.

[39] Z.X. Wang, C.X. Xu, L. Chen, J. Si, W.R. Li, S.S. Huang, Y. Jiang, Z.W. Chen, B. Zhao, In-situ lithiation synthesis of nano-sized lithium sulfide/grapheme aerogel with covalent bond interaction for inhibiting the polysulfides shuttle of Li-S batteries, *Electrochim. Acta* 312 (2019) 282-290.

[40] M.W. Xiang, L. Yang, Y.F. Zheng, J. Huang, P. Jing, H. Wu, Y. Zhang, H. Liu, A freestanding and flexible nitrogen-doped carbon foam/sulfur cathode composited with reduced graphene oxide for high sulfur loading lithium-sulfur batteries, *J. Mater. Chem. A* 5 (2017) 18020.

[41] Q.J. Shao, D.C. Guo, C. Wang, J. Chen, Yolk-shell structure MnO_2 @hollow carbon nanospheres as sulfur host with synergistic encapsulation of polysulfides for improved Li-S batteries, *J. Alloys Compd.* 842 (2020) 155790.

[42] J.H. Zhu, R. Pitcheri, T. Kang, C.M. Jiao, Y. Guo, J. Li, Y.J. Qiu, A polysulfide-trapping interlayer constructed by boron and nitrogen co-doped carbon nanofibers for long-life lithium sulfur batteries, *J. Electroanal. Chem.* 833 (2019) 151–159.

[43] Y. Kim, Y. Noh, H. Han, J. Bae, S. Park, S. Lee, W. Yoon, Y.K. Kim, H. Ahn, M.-H. Ham, W.B. Kim, Effect of N-doped carbon layer on Co_3O_4 nanowire-graphene composites as anode materials for lithium ion batteries, *J. Phys. Chem. Solids* 124 (2019) 266–273.

- [44] S.-D. Seo, C. Choi, B.-K. Kim, D.-W. Kim, Fabrication of highly porous carbon as sulfur hosts using waste green tea bag powder for lithium–sulfur batteries, *Ceram. Int.* 43 (2017) 2836–2841.
- [45] F. Qu, G. She, J. Wang, X. Qi, S. Li, S. Zhang, L. Mu, W. Shi, Coating nanoparticle–assembled Si microspheres with carbon for anode material in lithium–ion battery, *J. Phys. Chem. Solids* 124 (2019) 312–317.
- [46] F.R. Qin, K. Zhang, Z.A. Zhang, J. Fang, J. Li, Y.Q. Lai, H.T. Huang, Graphene/carbon aerogel for high areal capacity sulfur cathode of Li-S batteries, *Ionics* 25 (2019) 4615–4624.
- [47] K. Chen, Z.H. Sun, R.P. Fang, Y. Shi, H.M. Cheng, F. Li, Metal–organic frameworks (MOFs)–derived nitrogen–doped porous carbon anchored on graphene with multifunctional effects for lithium–sulfur batteries, *Adv. Funct. Mater.* 28 (2018) 1707592.
- [48] Y.G. Wang, Y. Lu, R.J. Luo, Y.G. Zhang, Y. Guo, Q.H. Yu, X.M. Liu, J.-K. Kim, Y.S. Luo, Densely-stacked N-doped mesoporous TiO₂/carbon microsphere derived from outdated milk as high-performance electrode material for energy storages, *Ceram. Int.* 44 (2018) 16265–16272.
- [49] D.W. Wang, G.M. Zhou, F. Li, K.H. Wu, G.Q. Lu, H.M. Cheng, I.R. Gentle, A microporous–mesoporous carbon with graphitic structure for a high–rate stable sulfur cathode in carbonate solvent–based Li–S batteries, *Phys. Chem. Chem. Phys.* 14 (2012) 8703–8710.
- [50] D. Li, F. Han, S. Wang, F. Cheng, Q. Sun, W.C. Li, High sulfur loading cathodes

fabricated using peapodlike, large pore volume mesoporous carbon for lithium–sulfur battery, *ACS Appl. Mater. Inter.* 5 (2013) 2208–2213.

[51] H.L. Wang, Y. Yang, Y.Y. Liang, J. Tucker Robinson, Y.G. Li, A. Jackson, Y. Cui, Graphene–wrapped sulfur particles as a rechargeable lithium–sulfur battery cathode material with high capacity and cycling stability, *Nano Lett.* 11 (2011) 2644–2647.

[52] X.J. Chen, G.H. Du, M. Zhang, A. Kalam, Q.M. Su, S.K. Ding, B.S. Xu, Nitrogen-doped hierarchical porous carbon derived from low-cost biomass pomegranate residues for high performance lithium-sulfur batteries, *J. Electroanal. Chem.* 848 (2019) 113316.

[53] P.Y. Li, J.N. Deng, J. Li, L.G. Wang, J.Q. Guo, Hollow graphene spheres coated separator as an efficient trap for soluble polysulfides in Li–S battery, *Ceram. Int.* 45 (2019) 13219–13224.

[54] H.L. Wu, L. Xia, J. Ren, Q.J. Zheng, F.Y. Xie, W.J. Jie, C.G. Xu, D.M. Lin, A multidimensional and nitrogen-doped graphene/hierarchical porous carbon as a sulfur scaffold for high performance lithium sulfur batteries, *Electrochim. Acta* 278 (2018) 83–92.

[55] Y.L. Yan, M.M. Shi, Y.M. Zou, Y.Q. Wei, L.P. Chen, C.J. Fan, R. Yang, Y.H. Xu, Tunable hierarchical porous carbon aerogel/graphene composites cathode matrix for Li-S batteries, *J. Alloys Compd.* 791 (2019) 952–961.

[56] C. Li, X.L. Sui, Z.B. Wang, Q. Wang, D.M. Gu, One-step synthesis of 3D N-doped graphene supported metal oxide for high performance Li-S battery, *Ceram. Int.* 44 (2018) 13419–13425.

- [57] L. Zhang, R.A. Senthil, J.Q. Pan, A. Khan, X. Jin, Y.Z. Sun, A novel carbon nanotubes@porous carbon/sulfur composite as efficient electrode material for high-performance lithium-sulfur battery, *Ionics* 25 (2019) 4761–4773.
- [58] G.Y. Xu, B. Ding, P. Nie, H.J. Luo, X.G. Zhang, Preparation and electrochemical performance of carbon nanotubes/graphene oxide/sulfur complex cathode material, *Acta Phys.-Chim. Sin.* 29 (2013) 546–552.
- [59] X.Z. Zhou, Q.R. Ma, S.R. Liang, F. Yang, X.F. Lu, Preparation and electrochemical performance of freeze-drying graphene coated sulfur/carbon cathode composites, *J. Northwest Normal Univ.: Nat. Sci.* 53 (2017) 58–77.
- [60] J.S. Lee, W. Kim, J. Jang, A. Manthiram, Sulfur-embedded activated multichannel carbon nanofiber composites for long-life, high-rate lithium–sulfur batteries, *Adv. Energy Mater.* 7 (2017) 1601943.
- [61] D.L. Chao, P. Liang, Z. Chen, L.Y. Bai, H. Shen, X.X. Liu, X.H. Xia, Y.L. Zhao, S.V. Savilov, J.Y. Lin, Pseudocapacitive Na–ion storage boosts high rate and areal capacity of self–branched 2D layered metal chalcogenide nanoarrays, *ACS Nano* 10 (2016) 10211–10219.
- [62] Y. Wu, W. Zhang, T.L. Han, Z.H. Shen, D. Cheng, H.K. Zhang, J.J. Li, H.G. Zhang, J.Y. Liu, A novel ternary sulfur/carbon@tin dioxide composite with polysulfides adsorptive shell and conductive core as high–performance lithium–sulfur battery cathodes, *Appl. Surf. Sci.* 489 (2019) 462–469.
- [63] H. Li, B. Zhang, X. Ou, L.B. Tang, C.H. Wang, L. Cao, C.L. Peng, J.F. Zhang, In-situ fabrication of hetero structured SnO_x@C/rGO composite with durable cycling life for improved lithium storage, *Ceram. Int.* 45 (2019) 18743–18750.

- [64] L. Qu, P. Liu, P. Zhang, T. Wang, Y.K. Yi, P. Yang, X.L. Tian, M.T. Li, B.L. Yang, Carbon-nanotube/sulfur cathode with in-situ assembled Si_3N_4 /graphene interlayer for high-rate and long cycling-life lithium-sulfur batteries, *Electrochim. Acta* 296 (2019) 155–164.
- [65] M.Y. Wang, S.H. Han, Z.S. Chao, S.Y. Li, B. Tan, J.X. Lai, Z.Y. Guo, X.L. Wei, H.G. Jin, W.B. Luo, W.J. Yi, J.C. Fan, Celgard-supported LiX zeolite membrane as ion-permselective separator in lithium sulfur battery, *J. Membrane Sci.* 611 (2020) 118386.
- [66] T.B. Zeng, P.H. Ji, B. Shang, Q.M. Peng, X.B. Hu, G. Li, Nano $\text{Li}_4\text{Ti}_5\text{O}_{12}$ as sulfur host for high-performance Li-S battery, *Ionics* 24 (2018) 2973–2982.
- [67] L.S. Ni, L.L. Jia, G. Chen, F.L. Wang, X.H. Liu, R.Z. Ma, Facile synthesis of porous FeCo_2O_4 nanowire arrays on flexible carbon cloth with superior lithium storage properties, *J. Phys. Chem. Solids* 122 (2018) 261–267.
- [68] L. Zhang, K. Shen, W. He, Y. Liu, L. Yin, S. Guo, Hierarchical nanorods constructed by $\text{Mn}_2\text{Mo}_3\text{O}_8$ @reduced graphene oxide nanosheet arrays with enhanced lithium storage properties, *J. Phys. Chem. Solids* 121 (2018) 71–77.
- [69] H.Y. Yan, X.X. Xue, Y.Q. Fu, X.M. Wu, J.W. Dong, Three-dimensional carbon nanotubes-encapsulated $\text{Li}_2\text{FeSiO}_4$ microspheres as advanced positive materials for lithium energy storage, *Ceram. Int.* 46 (2020) 9729–9733.
- [70] H.K. Zhang, J.Y. Liu, X.R. Lin, Y. Zhong, J.H. Ren, Z.L. Wang, T.L. Han, J.J. Li, A metal organic foam-derived zinc cobalt sulfide with improved binding energies towards polysulfides for lithium-sulfur batteries, *Ceram. Int.* 46 (2020) 14056–14063.

[71] M. Adam, P. Strubel, L. Borchardt, H. Althues, S. Dorfler, S. Kaske, Trimodal hierarchical carbide-derived carbon monoliths from steam- and CO₂-activated wood templates for high rate lithium sulfur batteries, *J. Mater. Chem. A* 3 (2015) 24103.

Figure captions

Fig. 1 Schematic illustration of synthesis procedure of MMMPC-rGO composite.

Fig. 2 (a, b) SEM images of MMMPC-rGO/NaCl. (c, d) SEM, (e) TEM and (f) HRTEM images of MMMPC-rGO. Inset shows SAED pattern of MMMPC-rGO.

Fig. 3 (a, b) SEM, (c) TEM and (d) HRTEM images of MPC-rGO. Inset shows SAED pattern of MPC-rGO.

Fig. 4 (a) Nitrogen adsorption/desorption isotherms of MMMPC-rGO, inset shows the pore size distribution of MMMPC-rGO. (b) XRD patterns of MMMPC-rGO/NaCl, MMMPC-rGO, MMMPC-rGO/S and sulfur.

Fig. 5 XPS spectra of MMMPC-rGO/S: (a) survey spectrum, (b) C 1s spectrum, (c) O 1s spectrum, and (d) S 2p spectrum.

Fig. 6 (a) Raman spectra of MMMPC-rGO, MMMPC-rGO/S and (b) TGA curves of MMMPC-rGO, MMMPC-rGO/S, MPC-rGO/S and commercial sulfur powder.

Fig. 7 (a) CV curves of MMMPC-rGO/S composites in potential range of 1.6-2.8 V at a scanning rate of 0.1 mV s^{-1} . (b) Charge/discharge profiles of MMMPC-rGO/S composites at 0.1 A g^{-1} . (c) Rate performance of MMMPC-rGO/S and MPC-rGO/S cathodes. Cycling capacity of MMMPC-rGO/S and MPC-rGO/S cathodes at (d) 0.1 A g^{-1} over 100 cycles, (e) 0.5 A g^{-1} over 200 cycles and (f) 1.0 A g^{-1} over 500 cycles.

Fig. 8 (a) CV curves of MMMPC-rGO/S composites at different scan rates ranging from 0.1 to 1 mV S^{-1} . (b) Plots of $\log i$ versus $\log v$. (c) Percentages of capacitive contribution at different scan rates for MMMPC-rGO/S cathode. (d) Plots of CV peak currents versus the square root of scan rate for anodic reaction of $\text{Li}_2\text{S}/\text{S}_8$ (Peak1) and cathodic reaction of $\text{S}_8/\text{Li}_2\text{S}_4$ (Peak2).

Fig. 9 Nyquist plots of MMMPC-rGO/S and MPC-rGO/S cathodes (a) before cycling test and (b) after 500 cycles. Insets are the corresponding simulation circuit models.

Figures

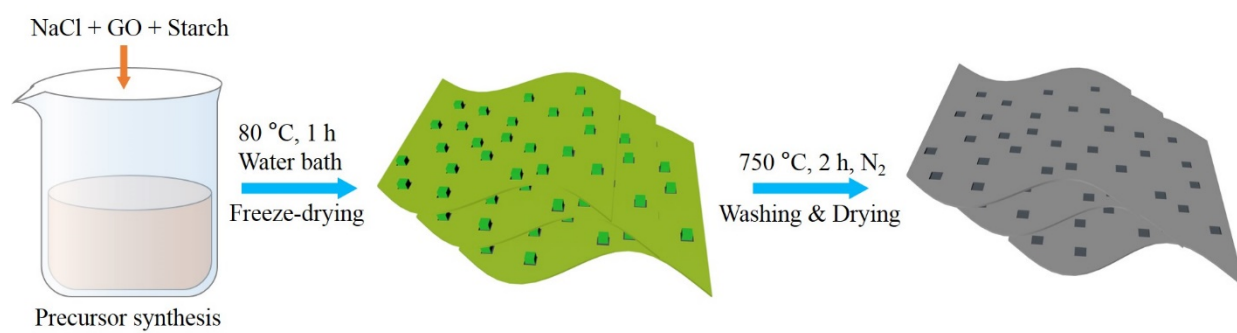


Fig. 1 Schematic illustration of synthesis procedure of MMMPC-rGO composite.

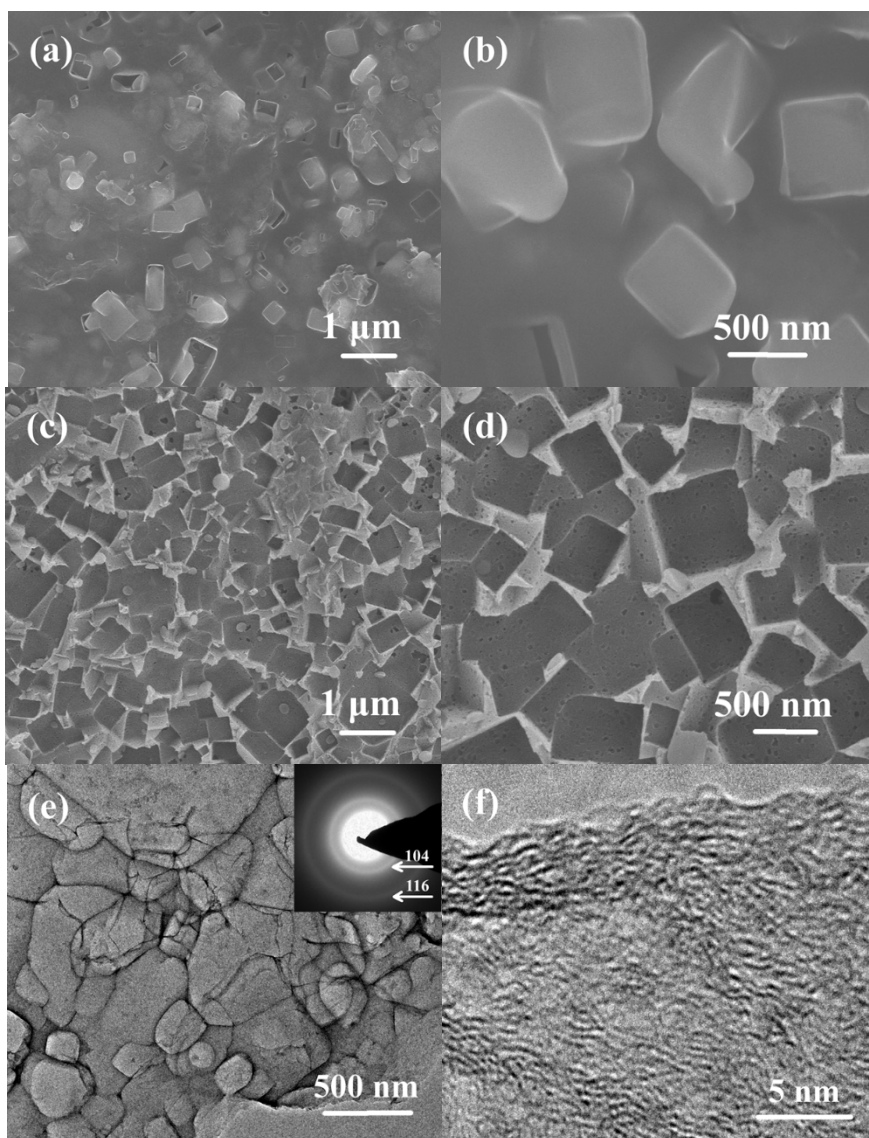


Fig. 2 (a, b) SEM images of MMMPC-rGO/NaCl. (c, d) SEM, (e) TEM and (f) HRTEM images of MMMPC-rGO. Inset shows SAED pattern of MMMPC-rGO.

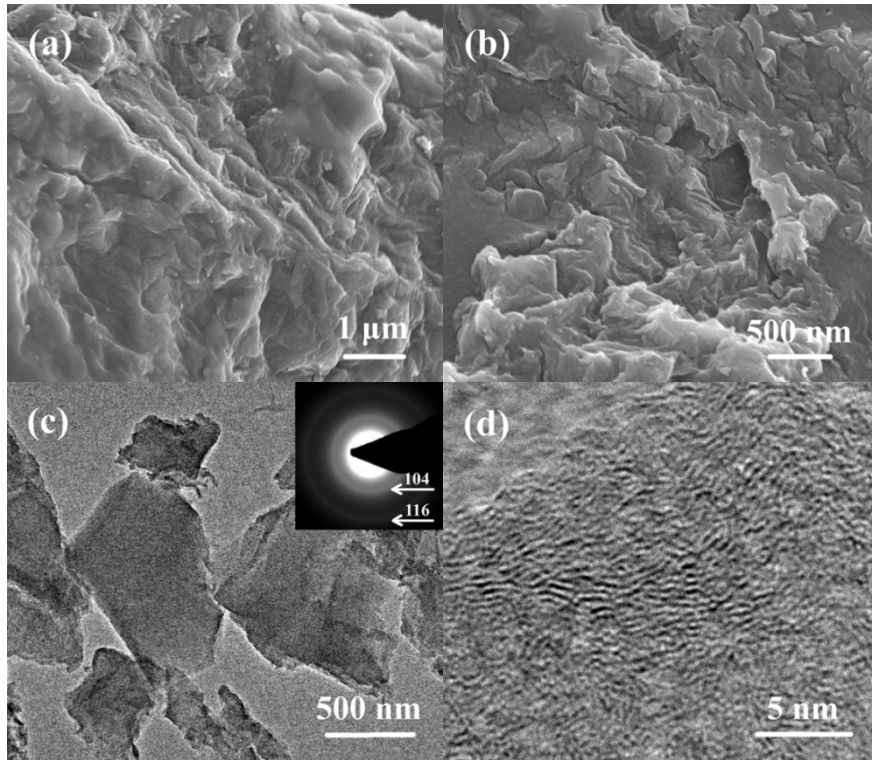


Fig. 3 (a, b) SEM, (c) TEM and (d) HRTEM images of MPC-rGO. Inset shows SAED pattern of MPC-rGO.

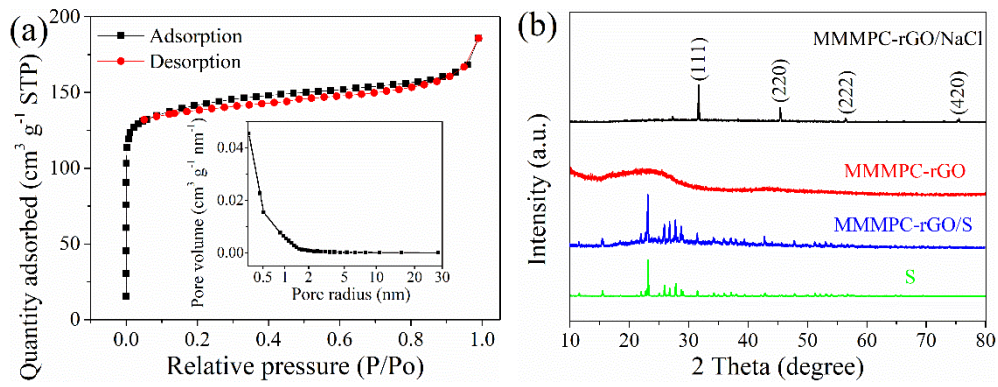


Fig. 4 (a) Nitrogen adsorption/desorption isotherms of MMMPC-rGO, inset shows the pore size distribution of MMMPC-rGO. (b) XRD patterns of MMMPC-rGO/NaCl, MMMPC-rGO, MMMPC-rGO/S and sulfur.

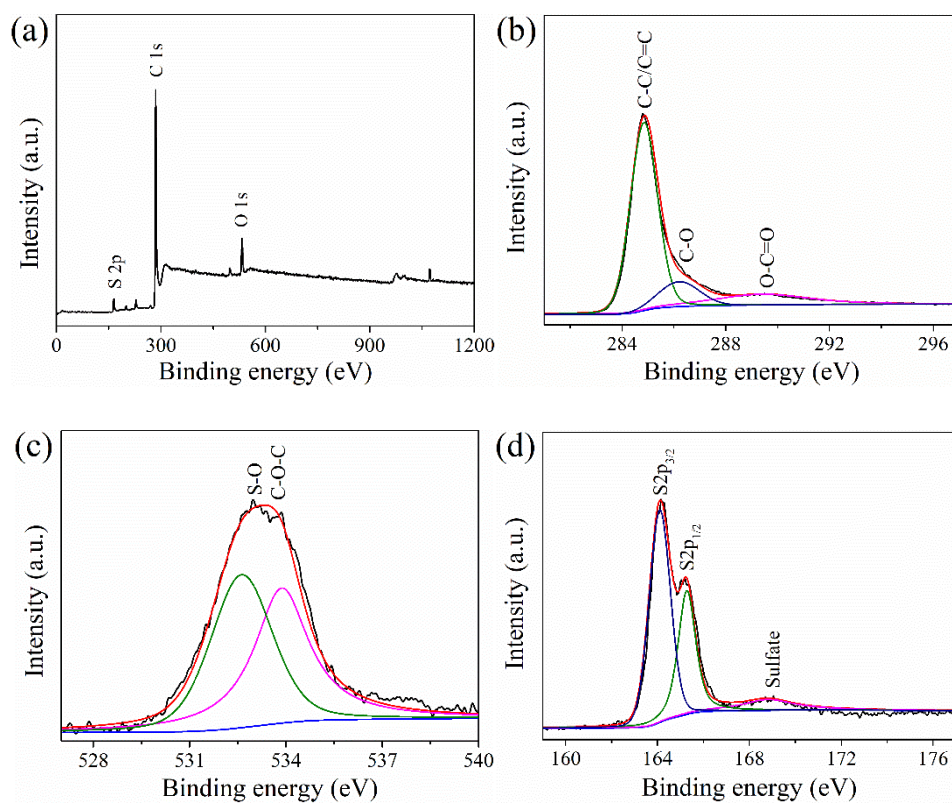


Fig. 5 XPS spectra of MMMPC-rGO/S: (a) survey spectrum, (b) C 1s spectrum, (c) O 1s spectrum, and (d) S 2p spectrum.

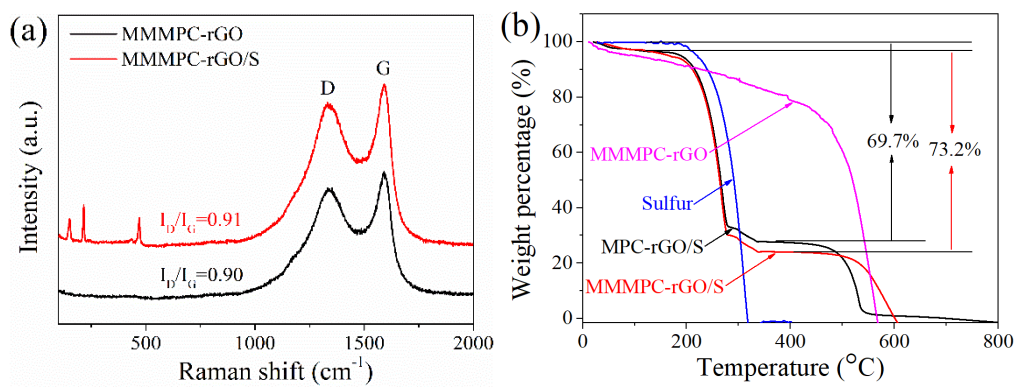


Fig. 6 (a) Raman spectra of MMMPC-rGO, MMMPC-rGO/S and (b) TGA curves of MMMPC-rGO, MMMPC-rGO/S, MPC-rGO/S and commercial sulfur powder.

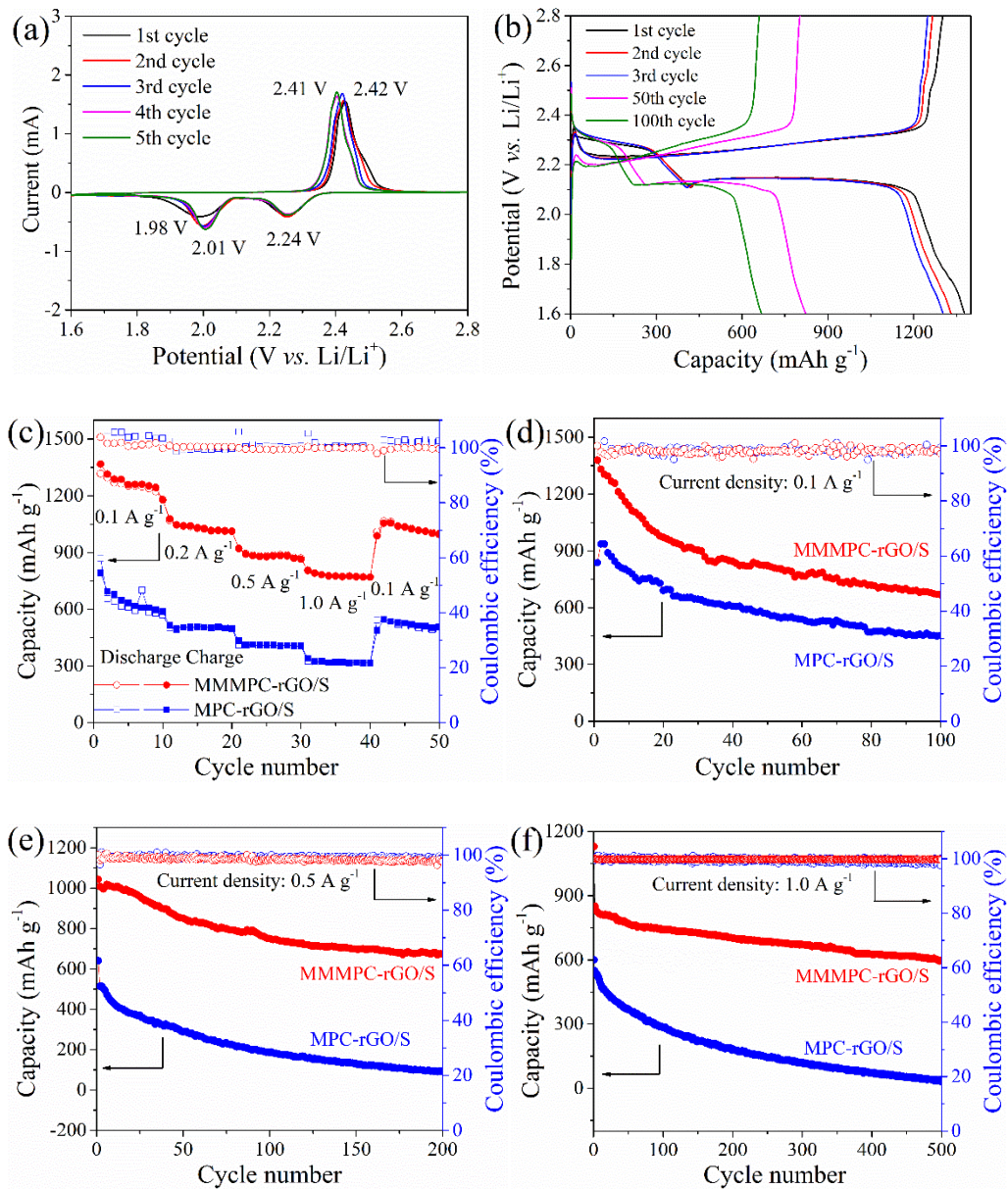


Fig. 7 (a) CV curves of MMMPC-rGO/S composites in potential range of 1.6-2.8 V at a scanning rate of 0.1 mV s⁻¹. (b) Charge/discharge profiles of MMMPC-rGO/S composites at 0.1 A g⁻¹. (c) Rate performance of MMMPC-rGO/S and MPC-rGO/S cathodes. Cycling capacity of MMMPC-rGO/S and MPC-rGO/S cathodes at (d) 0.1 A g⁻¹ over 100 cycles, (e) 0.5 A g⁻¹ over 200 cycles and (f) 1.0 A g⁻¹ over 500 cycles.

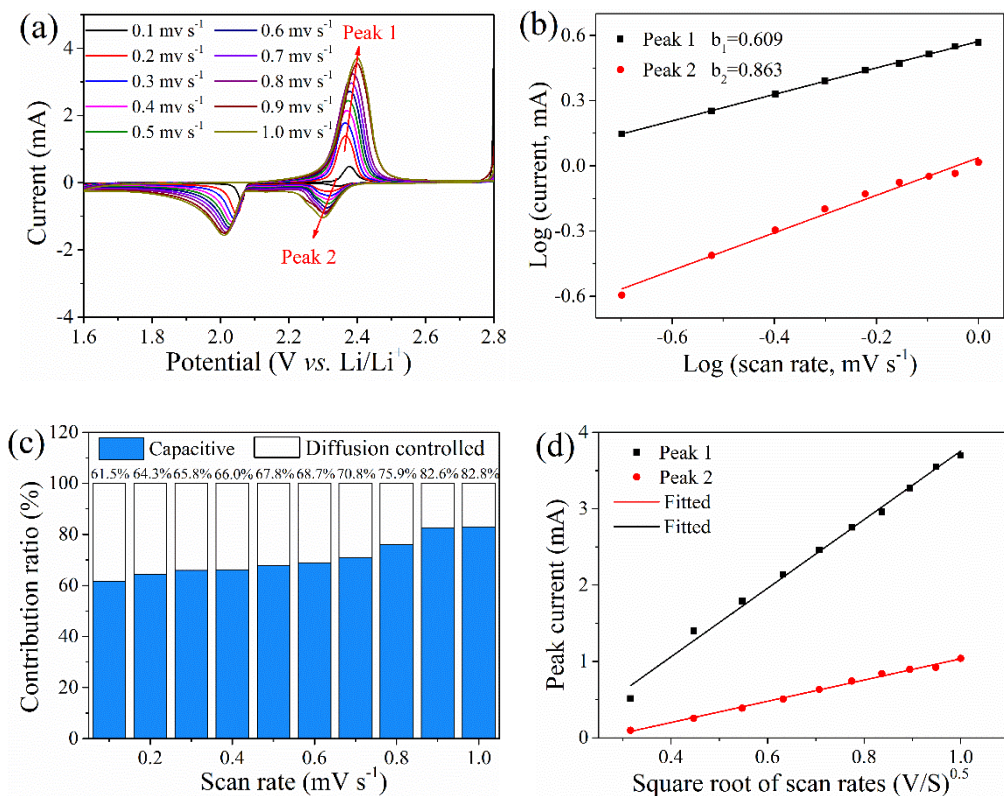


Fig. 8 (a) CV curves of MMMPC-rGO/S composites at different scan rates ranging from 0.1 to 1 mV S⁻¹. (b) Plots of log i versus log v . (c) Percentages of capacitive contribution at different scan rates for MMMPC-rGO/S cathode. (d) Plots of CV peak currents versus the square root of scan rate for anodic reaction of Li₂S/S₈ (Peak1) and cathodic reaction of S₈/Li₂S₄ (Peak2).

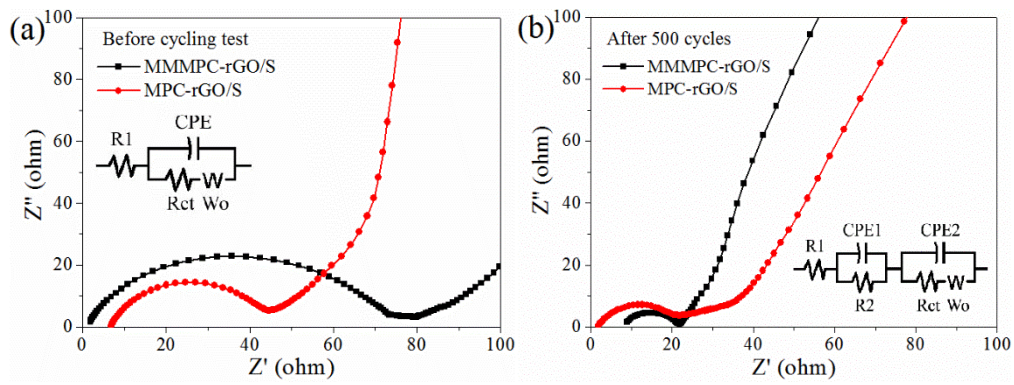


Fig. 9 Nyquist plots of MMMPC-rGO/S and MPC-rGO/S cathodes (a) before cycling test and (b) after 500 cycles. Insets are the corresponding simulation circuit models.